Available online at www.sciencedirect.com

International Journal of Heat and Fluid Flow 24 (2003) 584–595

International Journal of HEAT AND FLUID FLOW

www.elsevier.com/locate/ijhff

Large-eddy simulation of transonic turbulent flow over a bump

N.D. Sandham [a,*], Y.F. Yao [b], A.A. Lawal [a]

[a] *Aerodynamics & Flight Mechanics Research Group, School of Engineering Sciences, University of Southampton, Southampton SO17 1BJ, UK*
[b] *Alstom Power UK Ltd., P.O. Box 1, Waterside South, Lincoln LN5 7FD, UK*

Received 23 November 2002; accepted 5 March 2003

Abstract

Transonic turbulent boundary-layer flow over a circular-arc bump has been computed by high-resolution large-eddy simulation of the compressible Navier–Stokes equations. The inflow turbulence was prescribed using a new technique, in which known dynamical features of the inner and outer part of the boundary-layer were exploited to produce a standard turbulent boundary-layer within a short distance of the inflow. This method was separately tested for a flat plate turbulent boundary-layer, for which results compared well with direct numerical simulation databases. Simulation of the bump flow was carried out using high-order methods, with the dynamic Smagorinsky model used for sub-grid terms in the momentum and energy equations. Simulations were carried out at a Reynolds number of 233,000 based on bump length and free-stream properties upstream of the bump. At a back pressure equal to 0.65 times the stagnation pressure, a normal shock was formed near the bump trailing-edge and a peak mean Mach number of 1.16 was observed. Turbulence fluctuations decayed in the favourable pressure gradient region of the flow, before being amplified due to the shock interaction and boundary-layer separation. The effect of Reynolds number on turbulence intensity upstream of the shock is discussed in connection with a laminarisation parameter. With reference to turbulence modelling, anisotropy levels are not unreasonably high in the shock interaction region and shock unsteadiness was not found to be an issue. Of more relevance to the perceived poor performance of models for this type of flow may be the extremely rapid rise and decay of turbulence levels in the separated shear layer immediately under the shock-wave.

Keywords: Direct numerical simulation; Large-eddy simulation; Compressible turbulence; Shock/boundary-layer interaction

1. Introduction

Shock/boundary-layer interaction (SBLI) phenomena have important applications in a wide range of practical problems, such as transonic airfoils and wings, supersonic engine intakes, diffusers of centrifugal compressors, and turbo-machinery cascades. Pioneering research into SBLI was carried out by Liepmann (1946), who did the earliest experiments on laminar and turbulent boundary-layers interacting with a normal shock-wave. Since then considerable progress has been made towards understanding the complex interaction mechanisms. A review by Green (1970) summarized three major interaction scenarios: (i) a sharp compression corner generating an outgoing oblique shock-wave, (ii) the reflection of an incident oblique shock at a plane wall, and (iii) a weak normal shock-wave interacting with a spatially-developing boundary-layer, in which there is no curvature effect. For many practical flows, the interaction takes place at transonic speed on a curved surface, where the turbulent boundary-layer experiences large pressure gradients. Experimental investigations of shock/turbulent-boundary-layer interaction with non-zero pressure gradients have been carried out by Delery (1983) using a variable-curvature bump geometry, and by Liu and Squire (1988) using a circular-arc bump geometry. Both studies showed significant flow changes in the transonic regime, including a λ-shock pattern and extensive flow separation. Various techniques were used in the experiments in order to establish the details of both the mean flow and the turbulence. An additional study was made by Liu and Squire (1988) into the effect of curvature, using models of different radius and distinguishing between shock-induced separation and

---

[*] Corresponding author. Tel.: +44-23-8059-4872; fax: +44-23-8059-3058.

E-mail address: n.sandham@soton.ac.uk (N.D. Sandham).

doi:10.1016/S0142-727X(03)00052-3

bump trailing-edge separation (due to the adverse pressure gradient, independent of the shock).

With advances in computer technology and the development of suitable numerical algorithms, computation of SBLI has become feasible. The Reynolds-averaged Navier–Stokes (RANS) approach has been widely used and direct numerical simulation (DNS), with the advantages of resolving all scales of fluid motions, has also been adopted for the study of several model problems. Although DNS is limited to low Reynolds numbers and simple geometries, it offers a complete reference for the given flow, which is invaluable for understanding flow physics and assessing turbulence models. Adams (2000) carried out a direct simulation of turbulent boundary-layer flow over a compression corner at Mach number 3 and Reynolds number $Re_\theta = 1685$ (based on the inflow momentum thickness). A deflection angle of $\beta = 18°$ was chosen to generate a small (but more than incipient) flow separation, and a database was produced for model assessment. Numerical studies of an incident oblique shock-wave interacting with a two-dimensional laminar boundary-layer have been carried out by Katzer (1989) and Wasistho (1998). Further 3D studies are needed for strong interactions where the flow exhibits significant three-dimensionality and unsteady behaviour. Channel flow with the Delery (1983) bump geometry has been studied in some detail by RANS, for example Loyau et al. (1998) using a non-linear eddy-viscosity model and Batten et al. (1999) using a full Reynolds stress model. Unsatisfactory predictions of flows with significant SBLI is attributed to various deficiencies in the models, such as a failure to resolve anisotropy of the normal stresses. It is also a concern that steady state solvers will be in error if the flow is naturally unsteady and the shock location oscillates. Large-eddy simulation (LES) has not been widely applied to shock/boundary-layer interaction problems. Stolz et al. (2001) have demonstrated the potential for this approach using an approximate deconvolution subgrid model to obtain good comparisons with Adams' ramp flow DNS. Also Garnier et al. (2002) used LES to simulate shock impingement onto a turbulent boundary-layer at Mach 2.3. No simulations of the fully turbulent transonic bump flow problem have been published to date.

Recently Lawal and Sandham (2001) demonstrated the feasibility of a DNS approach for boundary-layer flow over the Delery bump with shock/laminar-boundary-layer interactions and flow transition to turbulence. In that study the upstream boundary-layer was laminar with transition triggered by a disturbance strip at the crest of the bump. The object of the present study is to extend the DNS/LES capability to turbulent boundary-layer flow over a bump geometry at transonic speed with turbulent shock/boundary-layer interactions.

2. Simulations

Both direct and large-eddy simulations have been run for this investigation. Key features of the code are described in this section together with details of the flow configuration chosen for study.

2.1. Governing equations and numerical method

We consider the motion of a Newtonian fluid, which is governed by the fundamental conservation laws for mass, momentum, and energy. In the following, we use an asterisk to denote dimensional quantities and a subscript '0' to denote stagnation quantities. Stagnation properties are a convenient reference for this flow since experiments are typically run by exhausting from an upstream reservoir of effectively stationary fluid. A thermally perfect gas with constant specific heat capacities (c_p at constant pressure and c_v at constant volume) is assumed and the ratio $\gamma = c_p/c_v$ is set to be 1.4. The non-dimensional viscosity μ (referenced to its value at the stagnation temperature) is assumed to satisfy the power law $\mu = T^{\Omega}$, where T is the non-dimensional temperature referenced to stagnation temperature with $\Omega = 0.76$. For convenience, tensor notation is used with subscripts 1, 2 and 3 representing the streamwise (x), wall-normal (y) and spanwise (z) coordinates respectively. Non-dimensionalization is carried out by

$$\rho = \rho^*/\rho_0^*, \quad u_i = u_i^*/a_0^*, \quad p = p^*/(\rho_0^* a_0^{*2}),$$
$$T = T^*/T_0^*, \quad E = E^*/(\rho_0^* a_0^{*2}).$$

Here, the terms ρ, u_i, p and E denote the density, three Cartesian velocity components, the pressure and the total energy ($E = p/(\gamma - 1) + \rho u_i u_i/2$), while a_0^* is the dimensional stagnation sound speed. Time is non-dimensionalized by δ_1^*/a_0^*, where δ_1^* is the dimensional inflow boundary-layer displacement thickness. The Reynolds number specified in the bump flow simulations is defined by $Re_0 = \rho_0^* a_0^* \delta_1^* / \mu_0^* = 5197$. For reasons of comparison with experiment we will also quote the Reynolds number based on δ_1^* and upstream flow properties, which is $Re = 2910$.

The compressible Navier–Stokes equations can be written in a compact notation as

$$\frac{\partial U}{\partial t} + \frac{\partial F^{\mathrm{I}}}{\partial x} + \frac{\partial G^{\mathrm{I}}}{\partial y} + \frac{\partial H^{\mathrm{I}}}{\partial z} = \frac{\partial F^{\mathrm{V}}}{\partial x} + \frac{\partial G^{\mathrm{V}}}{\partial y} + \frac{\partial H^{\mathrm{V}}}{\partial z}, \tag{1}$$

where the conservative variables are $U = [\rho, \rho u_i, E]^{\mathrm{T}}$. The convective and diffusive fluxes are F^{I}, G^{I}, H^{I} and F^{V}, G^{V}, H^{V} respectively. Details of these terms can be found in Sandham et al. (2002). A difference of the above formulation compared to Yao et al. (2000) is that pressure was there normalised with respect to p_0^* leading to extra factors of γ in the equations.

The principal issue in shock-wave/turbulence simulations is that good numerical methods for turbulence are generally inefficient for shock flows, while the best shock-capturing schemes are much too dissipative for accurate resolution of turbulence. Three main techniques are commonly used in shock–turbulence simulations: full shock resolution, essentially non-oscillatory (ENO) schemes, and hybrid methods, in which the method varies depending upon whether a shock-wave is detected. The former two methods have proved too expensive for routine calculations and consequently hybrid methods have most commonly been used. Recently a stable numerical method applying the concept of entropy splitting has been developed, in which 4th- or 6th-order (compact or non-compact) central differences were implemented together with a total variation diminishing (TVD) scheme with the artificial compression method (ACM) for detecting the shock-wave. In addition, a stable high-order numerical boundary treatment was used based on the summation by parts (SBP) approach of Carpenter et al. (1999). The idea of entropy splitting is to split the inviscid flux derivatives into a conservative part and a symmetric part based on an entropy variable. Experience shows that such a splitting procedure improves the non-linear stability and minimizes the numerical dissipation for both smooth flows and for problems with complex shock–turbulence interactions. The entropy splitting procedure was applied to the Euler terms given on the left hand side of Eq. (1) and details of the formulation can be found in Sandham et al. (2002). The shock-capturing algorithm is described in Yee et al. (1999).

Two numerical parameters are associated with the method and must be set for each simulation. A splitting parameter β fixes the proportions of conservative and symmetric formulations of the Euler terms. Enhanced non-linear stability is typically found for $1.25 < \beta < 12$ (Sandham et al., 2002), and we take $\beta = 4$ for simulations presented here. A shock-capturing parameter κ also needs to be specified. Despite the success of the ACM method in localising the effect of the extra dissipation to the immediate vicinity of the shock-wave, it is still advisable to keep κ as small as possible, without incurring oscillations near shock-waves. For mixing layer and shock tube problems we have typically employed $\kappa = 0.7$ (Yee et al., 1999; Lawal, 2002). For the current work we set $\kappa = 0$ for the shock-free turbulent boundary-layer and $\kappa = 0.2$ for the bump flow LES.

The simulation uses a parallel compressible LES/DNS code developed by Yao et al. (2000), which employs 4th-order central finite differences for spatial derivatives and a 3rd-order explicit Runge–Kutta algorithm for time advancement. Generalized coordinates are used so that complex geometries can be treated. Validations of the code have included vortex merging by Yee et al. (1999), shock tube flows by Lawal (2002), turbulent channel flow by Sandham et al. (2002) and supersonic turbulent boundary-layer flow by Li (2003).

For large-eddy simulation we consider the filtered Navier–Stokes equations, which contain extra terms that must be modelled, in particular the stress term

$$\bar{\rho}\tau_{ij} = \overline{\rho u_i u_j} - \overline{\rho u_i}\,\overline{\rho u_j}/\bar{\rho} \tag{2}$$

appears in both the momentum and energy equations. With the dynamic Smagorinsky model of Germano et al. (1991) the stress term is modelled by

$$\tau_{ij} = C_d \Delta^2 |S| S_{ij} \tag{3}$$

where C_d is a constant, to be defined dynamically, Δ is a filter width, and S_{ij} is the strain rate deduced from the density-weighted velocity field $\tilde{u}_i = \overline{\rho u_i}/\bar{\rho}$. In common with many other LES of wall-bounded turbulence we do not do any filtering in the wall-normal direction. The Lilly (1992) least-squares method of determining the constant is used. A top-hat filter with trapezoid integration is applied in physical space as the test filter of the dynamical procedure. This filter has width $\Delta = 2h$, where h is the grid spacing. In this case we have one homogeneous direction, so averaging is taken over that direction. Any negative values of the Smagorinsky constant C_d determined by this method are set to zero.

There are additional sub-grid terms in the energy equation (Vreman (1995) gives a complete list). At the low Mach numbers of transonic flow (peak Mach numbers 1.2, peak convective Mach number 0.6) it is unlikely that these will be significant. Nevertheless we include a modelling of these terms via an additional heat flux, which under our normalisation can be written as

$$q_i^{\mathrm{t}} = \frac{-C_d \bar{\rho} \Delta^2 |S|}{Pr_{\mathrm{t}}(\gamma - 1)} \frac{\partial T}{\partial x_i} \tag{4}$$

where the turbulent Prandtl number Pr_{t} is set to unity.

2.2. Problem definition

We consider compressible turbulent flow over a circular-arc bump geometry. When the back pressure is low enough compared to the upstream total pressure the incoming subsonic flow is accelerated over the bump to supersonic speeds. Over a certain range of back pressures, the supersonic flow is terminated by a nearly-normal shock located near the end of the bump. An interaction between the shock-wave and turbulent boundary-layer is then expected, as illustrated in Fig. 1(a). The flow separation can be caused either by the adverse-pressure-gradient at some distance before the shock, or by a strong shock/boundary-layer interaction at the shock foot, depending on the magnitude of the back pressure and the corresponding shock strength.

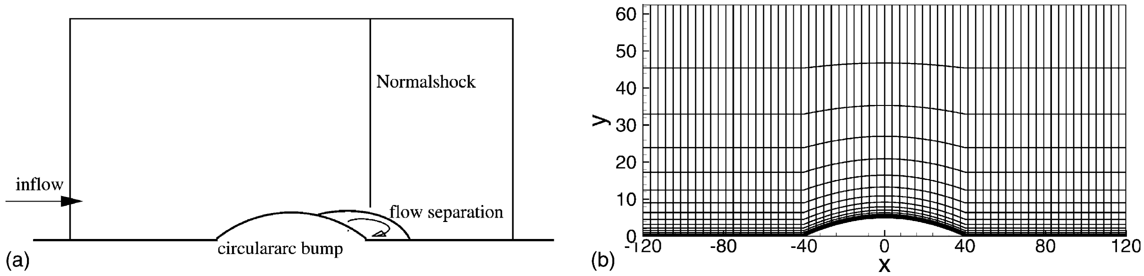

Fig. 1. Turbulent flow over a circular-arc bump: (a) a sketch of configuration; (b) typical computational grid (only a selection of grid lines are shown).

The inflow mean turbulent boundary-layer displacement thickness δ_1^* is taken equal to 1/5 of the bump height. The factor of 1/5 is chosen so that dimensionless distances in the simulation correspond numerically to dimensions in millimetres in the Liu and Squire (1988) experiments. The computational domain is then $240 \times 62.5 \times 16$ in the streamwise, wall-normal and spanwise directions respectively. The solution is assumed to be periodic in the spanwise direction. The circular-arc bump, which has a length of 80, a height of 5 and a radius of 163 (all based on δ_1^*), is located in the middle of the lower surface. The length of the up- and downstream flat plate is taken as 80. Grid points are uniformly distributed in the streamwise and spanwise directions and stretched in the wall-normal direction with more points clustered in the near-wall region. Fig. 1(b) shows a side-view of the computational domain.

The optimum choice of Reynolds number for the simulations turned out to be quite involved. Early work, as presented in Yao and Sandham (2002) used DNS at $Re = 1000$ based on incoming boundary-layer displacement thickness δ_1^* and free-stream flow conditions. For shock locations near the end of the bump, comparable to the Liu and Squire (1988) experiments, it was found that only slightly supersonic peak Mach numbers $M_\mathrm{p} = 1.05$ were obtained. Additionally, at this Reynolds number, there was a partial laminarisation of the flow near the top of the bump, leading to early separation of the boundary-layer. There was still sufficient turbulence in the flow to give a closed separation bubble comparable in length to that observed in experiments, however this was found to be sensitive to the upstream forcing. Despite flow phenomena involving laminarisation and re-transition being of considerable interest, it was decided additionally to attempt an LES at a higher Reynolds number (nominally 3000, in practice 2910 as the inflow velocity adjusts according to the back pressure). Results from this simulation, presented in this paper, are expected to be more representative of fully turbulent bump flow, despite the additional modelling errors introduced by moving from a DNS to an LES approach. The issue of laminarisation is discussed further in Section 4.3. The Reynolds number of 2910 based on inflow displacement thickness and free-stream conditions corresponds to $Re_0 = 5197$ with reference velocity taken as the stagnation sound speed. A Reynolds number based on bump length and free-stream properties is 233,000. This is still well below the original Liu and Squire (1988) experiments, where a comparable Reynolds number was 1.6×10^6, but does allow high-resolution LES to be made.

2.3. Boundary conditions

A proper description of turbulent inflow conditions is always a challenge for DNS. Previous studies, for example the compressible ramp flow (Adams, 2000) and the incompressible trailing-edge flow (Yao et al., 2001), used an additional precursor simulation to define the turbulent inflow. The method works well but at extra cost in CPU time, data storage and simulation complexity. In this simulation a new approach is used to prescribe the turbulent inflow, in which known dynamical features of the inner and outer part of the boundary-layer are reproduced, including lifted 'streaks' and coherent outer-layer motions, superimposed with random noise to break remaining symmetries. The method has first been tested for a zero-pressure-gradient turbulent boundary-layer and then used in the bump simulation.

At the subsonic inflow, the velocity is initially extrapolated from the interior. The computed total mass flow rate is then used in combination with the analytic turbulent mean velocity profile of Spalding (1961) (at the nominal Reynolds number $Re = 3000$) to give a complete inflow profile. Pressure and density in the free stream are computed by assuming isentropic flow from a reservoir to the inflow (Lawal, 2002). Fluctuations were introduced using the method described in the next section. At the subsonic outflow, the derivatives of density and three velocity components were assumed to be zero and a fixed back pressure was prescribed. At the lower wall, a no-slip condition was used for the velocity components and an isothermal wall condition was prescribed with a temperature equal to the stagnation temperature. At the upper surface, a free-slip boundary condition was applied. Periodic boundary conditions were used in the spanwise direction.

3. Turbulent boundary-layer flow

Simulation of a compressible turbulent boundary-layer at Mach number 0.6 and Reynolds number $Re = 1000$ (based on δ_1^* and the free-stream quantities) was carried out to validate a new method for prescribing turbulent inflow conditions. It is well understood that the inner layer of the turbulent boundary-layer has low speed streaks, which at high amplitude become unstable, while the outer layer has large scale coherent structures. In order to reproduce turbulent flow numerically, a fixed spectrum is commonly used. This method omits phase information and consequently it takes a long distance from the inflow to fully develop the turbulence. Here we follow a more deterministic approach and introduce specific inner- and outer-layer disturbances, with associated phase information. Disturbances in the inner region (denoted as $\hat{u}^{\text{inner}}$) are used to represent lifted streaks, with a peak at a location of $y^+_{\text{p},j}$, while the outer-region disturbances (denoted as $\hat{u}^{\text{outer}}$) represent three-dimensional vortices. The disturbances take the form:

$$\hat{u}^{\text{inner}} = c_{1,0}y^+ \text{e}^{-y^+/y^+_{\text{p},0}} \sin(\omega_0 t)\cos(\beta_0 z + \phi_0) \tag{5}$$

$$\hat{v}^{\text{inner}} = c_{2,0}(y^+)^2 \text{e}^{-(y^+/y^+_{\text{p},0})^2} \sin(\omega_0 t)\cos(\beta_0 z + \phi_0) \tag{6}$$

$$\hat{u}^{\text{outer}} = \sum_{j=1}^{3} c_{1,j} y/y_{\text{p},j} \text{e}^{-y/y_{\text{p},j}} \sin(\omega_j t)\cos(\beta_j z + \phi_j) \tag{7}$$

$$\hat{v}^{\text{outer}} = \sum_{j=1}^{3} c_{2,j} (y/y_{\text{p},j})^2 \text{e}^{-(y/y_{\text{p},j})^2} \sin(\omega_j t)\cos(\beta_j z + \phi_j) \tag{8}$$

where subscripts $j = 0, 1, 2, 3$ are mode indices, y^+ is the y-coordinate in wall units defined as $y^+ = \rho_\text{w} y u_\tau/\mu_\text{w}$ and the $c_{i,j}$ are constants. Forcing frequencies are denoted by ω_j, spanwise wave numbers by β_j, and phase shifts by ϕ_j. The spanwise velocity w is derived from a divergence-free condition, since we do not expect dilatational compressibility effects to appear until much higher Mach numbers than are studied here. Density and temperature fluctuations are expected to develop naturally once the turbulent velocity field is established.

For inner-layer disturbances, the characteristic frequency ω_j is estimated by assuming that the disturbance travels downstream for a distance of $\lambda_x^+ \simeq 500\pi$ at a convective velocity $U_\text{c} \simeq 10u_\tau$ within a complete time period (low speed plus high-speed streak), while the wave number β_j is derived by assuming a typical characteristic spanwise streak spacing of $\lambda_z^+ = 100$. For outer-layer disturbances, the characteristic frequency ω_j is estimated by assuming that the disturbance travels downstream for a distance of $\lambda_x \simeq 16$ at a velocity of about $0.75U_\infty$ within a complete time period. The wave numbers β_j are chosen to give a range of outer-layer structures with a scale up to the computational box size. Table 1 gives a summary of the parameters used in the demonstration flat plate boundary-layer simulation. The streamwise and wall-normal fluctuations were generated with one mode in the inner region and three modes in the outer region. Additional random noise with a maximum amplitude 4% of the free-stream velocity was used to break any remaining symmetries in the inflow condition.

To test the method, a computational domain of $50 \times 10 \times 8$ was used with a grid of $192 \times 96 \times 64$ points, uniformly distributed in the streamwise and spanwise directions and stretched in the wall-normal direction. The grid resolutions, estimated based on the inflow quantities, are $\Delta x^+ = 13.0$, $\Delta z^+ = 6.25$ and the first point is at about $y^+ = 0.92$ with a total of 10 points in the viscous sub-layer up to $y^+ = 10$. The simulation starts with a uniform flow field equal to the mean profiles of the inflow turbulence. The inflow turbulence fluctuations were introduced as described above. The simulation was initially run for 100 time units and statistical samples were accumulated for a further 100 time units, with a total of 4600 samples, using 32 processing elements (PE's) on an SGI Origin 3000 system. Fig. 2(a) shows a comparison of the simulated mean velocity profile with the law of wall and the incompressible DNS of Spalart (1988). Fig. 2(b) shows the turbulence intensities and Reynolds stress distributions using the defect coordinate (η), which compare well with the Spalart DNS data. Compressibility effects are not expected to be significant for this attached-flow simulation at Mach number 0.6. Improved comparisons are of course obtained if one moves further downstream, however the results shown here, obtained only $40\delta_1^*$ from the inflow, are already adequate for our purposes. A suitable turbulent boundary-layer has been obtained far sooner with this method than if one had started with laminar

Table 1
Parameters for inflow turbulent fluctuations for the turbulent boundary-layer test case

	j	$c_{1,j}$	$c_{2,j}$	ω_j	β_j	ϕ_j	$y^+_{\text{p},j}$	$y_{\text{p},j}$
Inner region	0	0.1	−0.0016	0.1	π	0.0	12	–
Outer region	1	0.3	−0.06	0.25	0.75π	0.0	–	1.0
	2	0.3	−0.06	0.125	0.50π	0.1	–	1.5
	3	0.3	−0.06	0.0625	0.25π	0.15	–	2.0

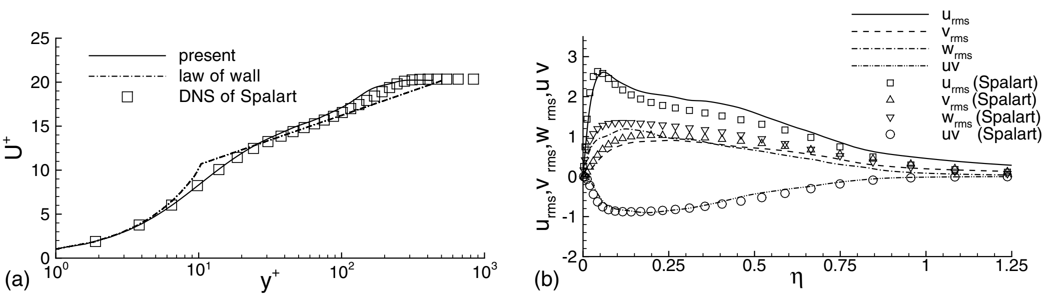

Fig. 2. Turbulent boundary-layer simulation results at $x \simeq 40\delta_1^*$. (a) Time- and spanwise-averaged mean velocity profile in wall units; (b) turbulence intensities and Reynolds stress distributions.

flow and forced transition via a time-varying wall-transpiration condition. The method has been extended to boundary-layer flow at Mach 2 by Li (2003).

4. Turbulent flow over a circular-arc bump

The large-eddy simulation of bump flow uses a computational domain of $240 \times 62.5 \times 16$ with a grid of $541 \times 161 \times 61$ points, uniformly distributed in the streamwise and spanwise directions and stretched (with a grid expansion factor of 1.035) in the wall-normal direction. At inflow the grid resolution is approximately $\Delta x^+ = 32$, $\Delta z^+ = 17$ with 15 points in the viscous sub-layer ($y^+ < 10$). Such a grid resolution is quite good for LES, since we are within a factor of two of DNS-type resolutions in horizontal directions, and better than many DNS in the wall-normal direction. At the worst location downstream where we have $\Delta x^+ = 49$, $\Delta z^+ = 28.5$ with 9 points in the viscous sub-layer. For the channel flow test case used by Sandham et al. (2002) with the present code, good turbulence results were obtained at such resolutions without any sub-grid model.

The simulation uses a length of $L_z = 16$ in the periodic spanwise direction. Based on the inflow mean 99.5% boundary-layer thickness $\delta_0 = 7.7$, the ratio of L_z/δ_0 is about 2.1, larger than the ratio of 1.22 used in DNS of ramp flow by Adams (2000), for which a two-point correlation study was carried out. For the reference inflow condition of Reynolds number $Re = 3000$, the spanwise length in wall units is about $L_z^+ = 1721$.

Table 2 shows the forcing constants for this case. Compared to the flat plate boundary-layer some of the constants were altered to account for the different boundary-layer Reynolds number and an extra outer-layer mode was added due to the spanwise box being chosen twice as wide as in the boundary-layer test case.

A fixed back pressure, equal to 0.65 times the stagnation pressure was prescribed. The simulation was then run for a time of 2800 (about 8 flow-through times) to set up the initial flow field and then statistical samples were accumulated for a further 1200 time units (3.3 flow-through times) with a total of 16,000 samples, using 128 PE's on an SGI Origin 3000 system.

4.1. Structure of the flow

The instantaneous Mach number and pressure contours, shown in side-view on Fig. 3, illustrate that a normal shock is formed at $x = 32$, close to the bump trailing-edge at $x = 40$. The developing turbulence fluctuations have been weakened in the first-half of the bump due to the favourable pressure gradient, but then re-develop in the second-half of the bump where an adverse pressure gradient exists. The fluctuations are greatly amplified after the separation.

Fig. 4 shows contour plots of the time- and span-averaged M, p, ρ and T. Despite the averaging the shock is still crisply captured in these views, indicating that outside the boundary-layer the flow is steady and spanwise-independent. The pressure and density plots show the beginnings of a λ-shock structure, with the front leg appearing as a weak Mach wave from just upstream of the separation point near $x = 9$. It should be noted how much the boundary-layer has thinned as it moves over the bump. At the top of the bump the 99%

Table 2
Parameters for inflow turbulent fluctuations in the bump simulation

	j	$c_{1,j}$	$c_{2,j}$	ω_j	β_j	ϕ_j	$y^+_{\mathrm{p},j}$	$y_{\mathrm{p},j}$
Inner region	0	0.08	−0.0014	0.38	2π	0.0	12	–
Outer region	1	0.3	−0.06	0.125	0.25π	0.1	–	1.0
	2	0.3	−0.06	0.0625	0.50π	0.2	–	1.5
	3	0.3	−0.06	0.031	0.75π	0.3	–	2.0
	4	0.3	−0.06	0.05	0.125π	0.4	–	1.5

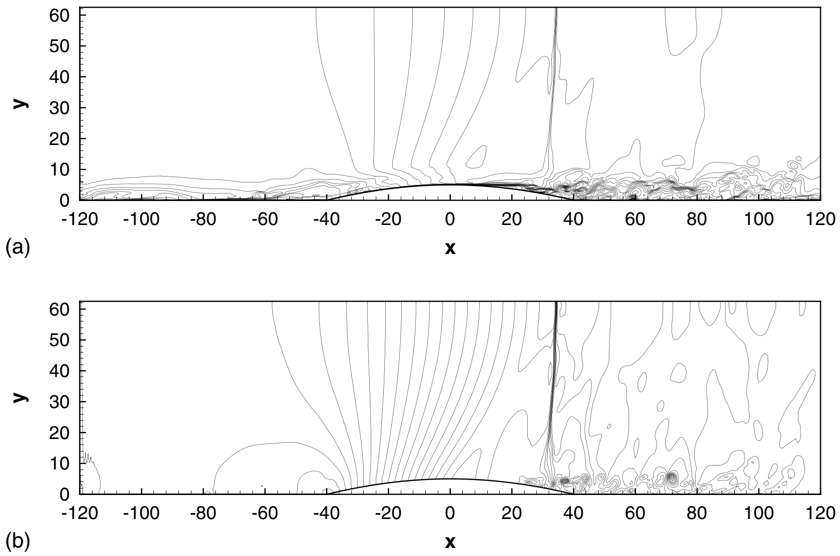

Fig. 3. Instantaneous views of (a) Mach number (max = 1.18, min = 0.0), and (b) pressure (max = 0.54, min = 0.30).

thickness is only around 0.5 and can barely be discerned on these plots. The peak Mach number is 1.16, obtained at $x = 32$, $y = 62.5$.

The skin friction (C_f) distribution along the streamwise direction, shown on Fig. 5(a), reveals many features of the flow. After a short transient where the skin friction recovers from the inflow condition it settles to a level around 0.0005. The influence of the bump starts to be felt at $x = -70$ and after $x = -60$ the skin friction drops sharply, going negative in the short separation bubble at the leading edge of the bump. Note that this circular-arc bump does not have any smoothing at the transition to the flat plate (in contrast to the Delery (1983) bump geometry). The skin friction increases rapidly over the bump as the boundary-layer thins. From Fig. 4(c) the pressure minimum is reached on the wall at $x = 4$ and thereafter a strong adverse pressure gradient serves to separate the boundary-layer at $x = 9$. The reattachment occurs downstream at $x = 50$ with the skin friction distribution in between quite typical of thin separation zones: an initial zone with small recirculation and barely negative skin friction, followed by a strong mean recirculation vortex above the largest negative values of skin friction. The skin friction relaxes downstream of the reattachment, reaching values of 0.006 by $x = 100$. The final rise at $x = 120$ is not physical, but due to the fixed back pressure applied at the outflow boundary. Fig. 5(b) shows the wall pressure (normalised by stagnation pressure) and Fig. 5(c) the free-stream Mach number distributions. The front part of the bubble is characterised by a plateau in the wall pressure. The pressure gradient downstream of the reattachment is mildly adverse initially, but then reduces to zero. The mean Mach number increases from 0.72 at the inflow to 1.16 at the maximum at $x = 32$. The largest streamwise gradient of the mean Mach number is seen near the crest of the bump. The pressure increase across the shock $p_2/p_1 = 1.40$ is consistent with the normal shock relation at $M = 1.16$ (with an identical $p_2/p_1 = 1.40$).

Although at a factor of nearly seven lower Reynolds number than the experiments of Liu and Squire (1988) it is worth making some quantitative comparisons. Compared to experiment the key difference is the location of separation. In the experiment, albeit with the shock in a slightly more rearward location, the separation is at $x \simeq 21$. This is an eighth of a bump length behind the LES with the consequence that in the experiment there is a greater turning angle of the flow at separation and consequently a stronger front leg of the λ shock. Bubble lengths are about the same since the experimental reattachment is further back by about 10 x-units compared to the simulation. The simulated wall pressures closely match the experimental values upstream and along the first-half of the bump. In the second-half of the bump the experimental wall pressure decreases for a longer distance than in the simulations due to the delayed separation. The peak Mach number (M_p) of the experiments is $M_p \simeq 1.27$, which is significantly higher than seen in the simulations and a consequence of the later separation.

4.2. Turbulence statistics

Fig. 6(a) shows the simulated mean velocity profiles at ten different downstream locations. Noteworthy features include the extreme thinning of the boundary-layer at the top of the bump $x = 0$, the reverse flow (maximum magnitude around 16% of the local free stream) for

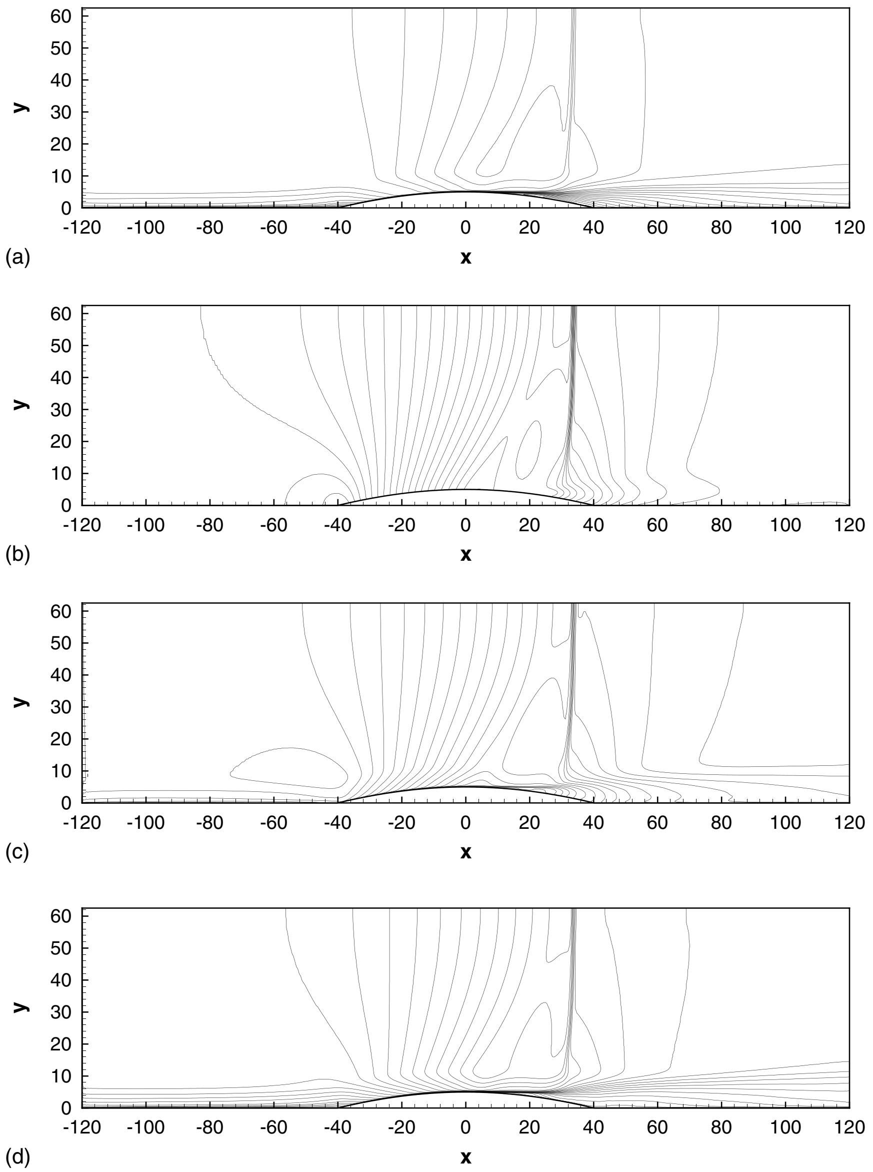

Fig. 4. Contour plots of mean values of (a) Mach number (max = 1.16, min = 0.0), (b) pressure (max = 0.53, min = 0.31), (c) density (max = 0.79, min = 0.44) and (d) temperature (max = 1.00, min = 0.78).

$20 < x < 40$, and the recovery for $x > 60$. Selected profiles are plotted in wall units u^+ against y^+ on Fig. 6(b), compared with a standard law of the wall $u^+ = 2.44 \log y^+ + 5.0$. Due to the low Mach numbers it was not considered necessary to apply any van Driest-type normalisation. It can be seen that at the top of the bump the boundary-layer profile is reduced to a total thickness $\delta^+ \simeq 60$ with an edge velocity $U_e^+ \simeq 20$. In the recovery region downstream of reattachment we see profiles that are changing quite rapidly, with a trend for the large wake component to reduce. For example U_e^+ reduces from 47 at $x = 60$ to 34 at $x = 100$. The domain is not long enough to see complete relaxation to an equilibrium turbulent boundary-layer. For comparison the shape factor of the boundary-layer (with integrations carried up to the point where the velocity profiles first reach 99% of the value on the upper boundary) is 1.49 at inflow, 1.36 at the top of the bump, 2.44 at $x = 60$, reducing to 1.68 at $x = 100$.

Contour plots of the root-mean-square (RMS) turbulence fluctuations u_{RMS} v_{RMS} and w_{RMS} are shown on Fig. 7(a)–(c) with the Reynolds stress $-\langle u'v' \rangle$ shown on Fig. 7(d). These plot are dominated by the behaviour of the turbulence downstream of separation and especially in the recirculation region. Peak values are seen at $x = 30$ in the middle of the separated shear layer immediately under the foot of the main shock-wave. Profiles of these turbulence quantities are shown at x locations of −120, 0, 30, 60 and 100 on Fig. 8. The RMS turbulence quantities are reduced by a factor of about

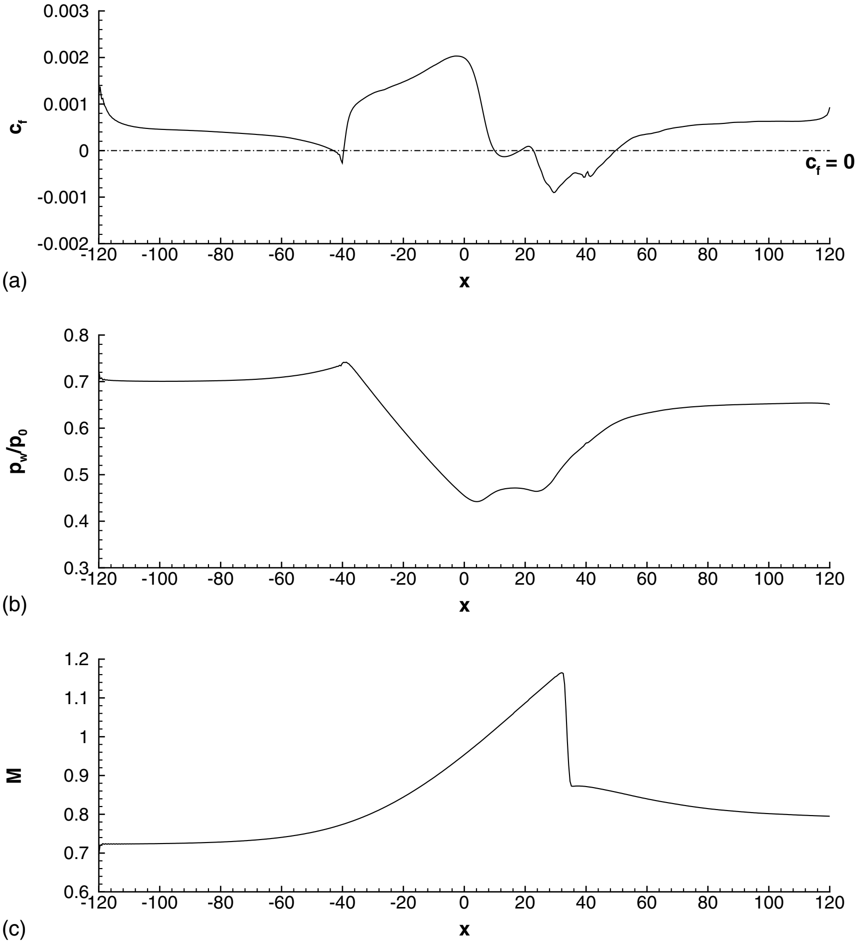

Fig. 5. Streamwise (x) variation of (a) skin friction (wall shear stress normalised by $0.5\rho_0^* a_0^{*2}$), (b) wall pressure p_w/p_0 and (c) free-stream Mach number.

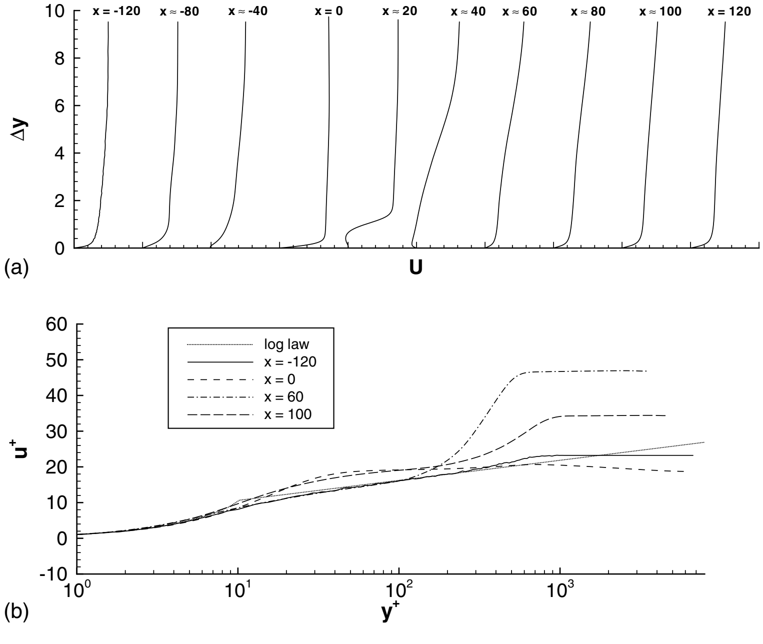

Fig. 6. Mean velocity profiles (a) at different x-locations and (b) in wall units.

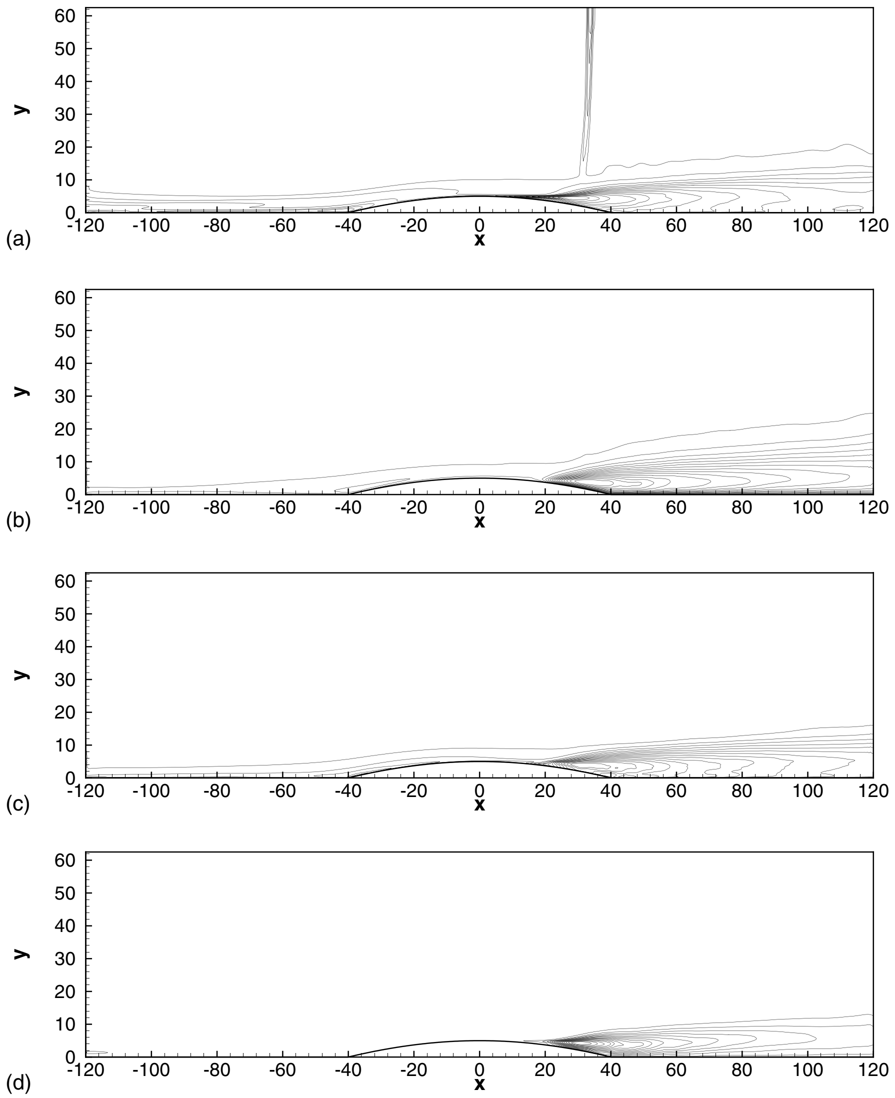

Fig. 7. Contour plots of turbulence quantities (a) u_{RMS} (max = 0.25, min = 0), (b) v_{RMS} (max = 0.16, min = 0), (c) w_{RMS} (max = 0.18, min = 0) and (d) $-\langle u'v' \rangle$ (max = 0.02, min = 0).

three relative to the inflow by the top of the bump, but then increase rapidly. At $x = 60$ after reattachment the RMS turbulence quantities are still four times inflow levels, reducing by a factor of two by $x = 100$.

A failure to model anisotropy of turbulence is a possible factor in the poor performance of turbulence models for SBLI problems. However here we do not see very extreme values. The ratio of peak values of u_{RMS}:v_{RMS}:w_{RMS} is 1.42:0.90:1 at $x = 30$, 1.21:0.95:1 at $x = 60$ and 1.26:1.05:1 at $x = 100$. Obviously the anisotropy in the very near-wall region is much higher, but this is well known and does not prevent good predictions from models of equilibrium flat plate boundary-layer flows. Of more relevance to the perceived poor performance of models for this type of flow may be the extremely rapid rise and decay of turbulence levels in the separated shear layer immediately under the shock-wave.

4.3. Potential for laminarisation

A widely-used acceleration parameter that can be linked to laminarisation (see for example Jones and Launder, 1972) is

$$K = \frac{\mu_e}{\rho_e U_e^2} \frac{\mathrm{d}U_e}{\mathrm{d}x}, \tag{9}$$

where a subscript e denotes free-stream properties, the criterion for laminarisation is roughly $K > 3 \times 10^{-6}$, although this depends on the streamwise extent for which the favourable pressure gradient is sustained, and presumably also on the Reynolds number. The value of K in our simulations depends on the wall-normal location. If this is taken at the upper boundary of the simulation we have $K_{\max} = 1.65 \times 10^{-6}$ and if it is taken at a distance $\Delta y = 20$ above the surface we have $K_{\max} = 2.35 \times 10^{-6}$. (The contribution from the wall-normal

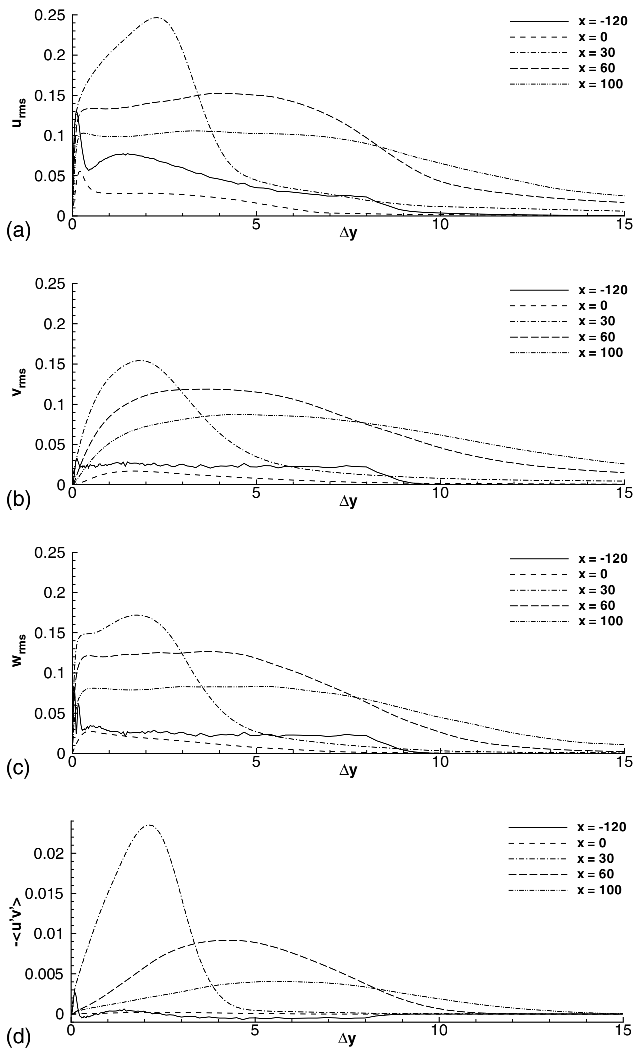

Fig. 8. Profiles through the turbulence data at $x = -120, 0, 30, 60, 100$: (a) u_{RMS}, (b) v_{RMS}, (c) w_{RMS} and (d) $-\langle u'v' \rangle$.

component of velocity has been neglected for this calculation.) We conclude that laminarisation should not be an issue here. However, we can see that at the Reynolds numbers used for previous DNS calculations of Yao and Sandham (2002) the criteria would be exceeded locally, even if there is not a sufficient streamwise length of exposure to this level of K to cause a complete laminarisation of the boundary-layer. It is concluded that the present simulations are just in excess of the minimum Reynolds number for fully turbulent bump flow. Full DNS of this case would require a factor of about four more grid points in x and z. Obviously this is expensive, and our current thoughts are that DNS studies of fully turbulent SBLI are probably better focused on ramp and shock impingement test cases. The current case remains a good case for comparative testing of subgrid models and numerical parameters in LES at lower resolutions, since it contains a variety of different physical phenomena (multiple separations, shock interactions, boundary-layer response to pressure gradient), all of which have to be accurately computed simultaneously.

5. Conclusions

The feasibility of LES for applications to turbulent boundary-layer flow over a circular-arc bump geometry, including shock/turbulent-boundary-layer interactions has been demonstrated. A new technique for time-dependent inflow conditions was described. This works well for both flat plate turbulent boundary-layer and turbulent circular-arc bump flows, generating fully-developed turbulence more quickly than full simulation of transition from laminar flow. The bump simulation was carried out with LES in a Reynolds-number regime above that where laminarisation may be an issue. Data from the simulation exhibit some differences compared to the much higher Reynolds number Liu and Squire experiment, the most significant being the earlier flow separation and lower peak Mach number. The simulation shows that the shock is steady and the level of anisotropy in the reattached flow are not excessively high. It is concluded that turbulence model performance is limited here by the need to capture the rapid rise and fall of turbulence levels in the separated shear layer under the root of the main shock-wave.

Acknowledgements

Financial support by the UK Engineering and Physical Science Research Council (EPSRC) through the research grants GR/M 84336 and GR/R 64957 (computer time) is gratefully acknowledged.

References

Adams, N.A., 2000. Direct simulation of the turbulent boundary layer along a compressible ramp at $M = 3$ and $Re_\theta = 1685$. Journal of Fluid Mechanics 420, 47–83.

Batten, P., Craft, T.J., Leschziner, M.A., Loyau, H., 1999. Reynolds-stress-transport modeling for compressible aerodynamics applications. AIAA Journal 37 (7), 785–797.

Carpenter, M.H., Nordstrom, J., Gottlieb, D., 1999. A stable and conservative interface treatment of arbitrary spatial accuracy. Journal of Computational Physics 148 (2), 341–365.

Delery, J.M., 1983. Experimental investigation of turbulence properties in transonic shock/boundary-layer interactions. AIAA Journal 21 (2), 180–185.

Garnier, E., Sagaut, P., Deville, M., 2002. Large eddy simulation of shock/boundary-layer interaction. AIAA Journal 40 (10), 1935–1944.

Germano, M., Piomelli, U., Moin, P., Cabot, W.H., 1991. A dynamic subgrid-scale eddy viscosity model. Physics of Fluids A 3, 1760–1765.

Green, J.E., 1970. Interactions between shock waves and turbulent boundary layers. Progress in Aerospace Sciences 11, 235–340.

Jones, W.P., Launder, B.E., 1972. The prediction of laminarization with a two-equation model of turbulence. International Journal of Heat and Mass Transfer 15, 301–314.

Katzer, E., 1989. On the lengthscales of laminar shock/boundary-layer interaction. Journal of Fluid Mechanics 206, 477–496.

Lawal, A.A., 2002. Direct numerical simulation of transonic shock/boundary-layer interactions. PhD Thesis, University of Southampton.

Lawal, A.A., Sandham, N.D., 2001. Direct simulation of transonic flow over a bump. In: Geurts, B.J. et al. (Eds.), Direct and Large-Eddy Simulation IV. pp. 301–310.

Li, Q., 2003. PhD Thesis, University of Southampton.

Liepmann, H.W., 1946. The interaction between boundary layer and shock waves in transonic flows. Journal of Aerospace Sciences 13 (12), 623–638.

Lilly, D.K., 1992. A proposed modification of the Germano subgrid-scale closure method. Physics of Fluids A 4, 633–635.

Liu, X., Squire, L.C., 1988. An investigation of shock boundary-layer interactions on curved surfaces at transonic speeds. Journal of Fluid Mechanics 187, 467–486.

Loyau, H., Batten, P., Leschziner, M.A., 1998. Modelling shock/boundary-layer interaction with nonlinear eddy-viscosity closures. Journal of Flow, Turbulence and Combustion 60 (3), 257–282.

Sandham, N.D., Li, Q., Yee, H.C., 2002. Entropy splitting for high-order numerical simulation of compressible turbulence. Journal of Computational Physics 178 (2), 307–322.

Spalart, P.R., 1988. Direct simulation of a turbulent boundary layer up to $Re_\theta = 1410$. Journal of Fluid Mechanics 187, 61–98.

Spalding, D.B., 1961. A single formula for the law of the wall. Journal of Applied Mechanics 83, 455–458.

Stolz, S., Adams, N.A., Kleiser, L., 2001. The approximate deconvolution model for large eddy simulations of compressible flow and its application to shock-turbulent-boundary-layer interaction. Physics of Fluids 13 (10), 2985–3001.

Vreman, B., 1995. Direct and large-eddy simulation of the compressible turbulent mixing layer. PhD Thesis, University of Twente, The Netherlands.

Wasistho, B., 1998. Spatial direct numerical simulation of compressible boundary layer flow. PhD Thesis, University of Twente, The Netherlands.

Yao, Y.F., Sandham, N.D., 2002. Direct numerical simulation of turbulent flow over a bump with shock/boundary-layer interactions. ETMM5 Conference, Majorca, Spain, Sept. 2002.

Yao, Y.F., Lawal, A.A., Sandham, N.D., Wolton, I.C., Ashworth, M., Emerson, D.R., 2000. Massively parallel simulation of shock/boundary-layer Interactions. In: Proc. Inter. Conf. Applied Computational Fluid Dynamics, Beijing. pp. 728–735.

Yao, Y.F., Thomas, T.G., Sandham, N.D., Williams, J.J.R., 2001. Direct numerical simulation of turbulent flow over a rectangular trailing edge. Theoretical and Computational Fluid Dynamics 14, 337–358.

Yee, H.C., Sandham, N.D., Djomehri, M.J., 1999. Low-dissipative high-order shock-capturing methods using characteristic-based filters. Journal of Computational Physics 150, 199–238.